Journal of Hydraulic Research, 2019
https://doi.org/10.1080/00221686.2019.1671511

Research paper

Efficient numerical representation of the impacts of flexible plant reconfiguration on canopy posture and hydrodynamic drag

AMIR MEHDI RAZMI, Postdoctoral Researcher, Laboratory of Hydraulics, *The Parsons Laboratory for Environmental Science and Engineering, Department of Civil and Environmental Engineering, Massachusetts Institute of Technology, Cambridge, MA, USA*; *Hydrology and Glaciology, Department of Civil, Environmental and Geomatic Engineering, Swiss Federal Institute of Technology in Zurich, Switzerland*
Emails: arazmi@mit.edu, razmi@vaw.baug.ethz.ch (author for correspondence)

MARCELO CHAMECKI, Associate Professor, *Department of Atmospheric and Oceanic Sciences, University of California, Los Angeles, CA, USA*
Email: chamecki@ucla.edu

HEIDI MARGARET NEPF (IAHR Member), Professor, *The Parsons Laboratory for Environmental Science and Engineering, Department of Civil and Environmental Engineering, Massachusetts Institute of Technology, Cambridge, MA, USA*
Email: hmnepf@mit.edu

ABSTRACT
This study considered a new approach for representing flexible canopies within large-eddy simulation that captures the impacts of reconfiguration on both the canopy posture and the canopy drag. The unsteady change in plant posture in response to the passage of turbulence structures (*monami*) was assessed using established steady-reconfiguration models responding to the unsteady velocity at the top of the canopy. The new drag and plant posture models improved the modelling of highly flexible canopies by more accurately capturing the observed vertical distribution of peak Reynolds stress. When compared to models that do not consider reconfiguration, or that represent it only through a velocity-dependent drag coefficient, the addition of a velocity-dependent canopy posture (unsteady reconfiguration) achieved up to a 56% reduction of the root mean square error for mean horizontal flow velocity and Reynolds stress profiles over the canopy. The RMSE for turbulence intensities and skewness were reduced up to 48% and 56%, respectively.

Keywords: Distributed drag force; flexible vegetation; monami; plant–flow interaction; reconfiguration; turbulence

1 Introduction

By stabilizing the bed, filtering nutrients, producing oxygen, providing habitat and promoting carbon sequestration, submerged, aquatic vegetation, such as seagrass, delivers important ecological and economical services that make it a vital part of freshwater or coastal ecosystems (Barbier et al., 2011). Seagrass commonly exists in canopies, i.e. close groupings of individual plants. The dynamic interaction of the canopy and the flow influence the retention of particles within the canopy, which in turn impacts water clarity and carbon sequestration (Kennedy et al., 2010). Aquatic vegetation worldwide is in decline due to changing climate and anthropogenic pressure (Waycott et al., 2009). The rate of seagrass loss has accelerated in recent decades, increasing from 0.9% yr^{-1} before 1940 to 7% yr^{-1} since 1970 (Waycott et al., 2009). A better understanding of how seagrass canopies interact with waves and currents could improve restoration strategies and coastal management. The goal of this study is to evaluate different vegetation drag models for application in large-eddy simulation (LES) modelling. This study describes an efficient way to represent the impact of unsteady blade reconfiguration on canopy height, canopy frontal area distribution and canopy drag coefficient within the framework of a distributed drag model.

As flow passes through a vegetation canopy, drag forces acting at the surfaces of canopy elements dissipate flow

Received 2 July 2018; accepted 16 September 2019/Currently open for discussion.

ISSN 0022-1686 print/ISSN 1814-2079 online
http://www.tandfonline.com

momentum. A distributed drag force can represent this impact of the canopy on the flow. For flexible canopies, the drag imparted by the individual blades on the flow can be altered by blade reconfiguration, i.e. the bending of individual blades in response to flow (e.g. Luhar & Nepf, 2011). Further, in sufficiently dense canopies, the discontinuity of drag at the top of the canopy leads to an inflection point in the velocity profile, which gives rise to Kelvin–Helmholtz (KH) vortices (also called coherent eddy structures). These vortices are maintained by the shear at the top of the canopy and move progressively downstream (Raupach, Finnigan, & Brunet, 1996). If the plants are flexible, the passage of these vortices creates a progressive waving of the vegetation, which in seagrass canopies is called *monami*, and the bending of the canopy has been shown to reduce the canopy drag (e.g. Ghisalberti & Nepf, 2002).

Flow through vegetation canopies has been studied with Reynolds-averaged models (e.g. King, Tinoco, & Cowen, 2012). However, these models only simulate mean fields, and fail to capture the impact of coherent structures, such as the KH vortices generated at the canopy interface. In contrast, LES explicitly resolves eddy motions that contribute to the unsteady velocity field. In flexible canopies, the unsteady velocity field can produce unsteady reconfiguration of plant elements, which in turn impacts the drag on individual coherent structures (Marjoribanks, Hardy, Lane, & Parsons, 2014; Pan, Chamecki, & Isard, 2014). The need to include plant reconfiguration and its impact on canopy drag led to numerical approaches that resolved each flexible plant, hereafter referred to as the plant-scale approach (Dupont et al., 2010; Ikeda, Yamada, & Toda, 2001; Li & Xie, 2011; Marjoribanks et al., 2014; Mattis, Dawson, Kees, & Farthing, 2015). In these approaches, the reconfiguration of individual plants was directly modelled, and the feedback to the flow was represented with different levels of complexity. The flow and plant posture details provided in these studies has advanced our understanding of plant–flow interaction. However, these approaches demand vast computational resources, because they resolve the unsteady motion of each individual plant. Because of the high computational cost, it is impossible to numerically model a large scale canopy, limiting the practical applications of this method.

Several previous studies have described other methods for predicting velocity profiles within and above aquatic canopies, but these have been based on a rigid canopy (e.g. Huthoff, Augustijn, & Hulscher, 2007; Katul, Poggi, & Ridolfi, 2011). Nikora, Nikora, and Donoghue (2013) provided a conceptual model for flows with flexible vegetation. Nezu and Sanjou (2008) used LES to simulate the coherent structures in aquatic canopy flows. However, their model treated the vegetation as a rigid canopy, neglecting the effects of vegetation reconfiguration. Importantly, Nezu and Sanjou (2008) noted that the inclusion of vegetation flexibility, as this paper considers, was needed to capture more realistic aquatic canopy flow.

The idea of using a distributed drag force to represent vegetation was suggested by Burke and Stolzenbach (1983) for modelling flow through marsh grasses and by Shaw and Schumann (1992) for modelling a forested boundary. Many authors have used this approach for modelling canopy flows (e.g. Choi & Kang, 2016; Gerken, Chamecki, & Fuentes, 2017; Lien, Yee, & Wilson, 2005; Yan, Nepf, Huang, & Cui, 2017). Pan, Chamecki, et al. (2014) modified the distributed drag model for a corn canopy to capture the impact of leaf reconfiguration on canopy drag. Specifically, to mimic the reduction in drag coefficient with increasing leaf reconfiguration, the drag coefficient was set to decrease with increasing, instantaneous, local velocity. The present paper considers an extension of the Pan, Chamecki, et al. (2014) model to seagrass. The extension is not straightforward, because seagrass is significantly more flexible than corn, and the reconfiguration of individual blades impacts not only the drag coefficient, but also the frontal area distribution and the canopy height. To explore each impact in turn, we consider a set of progressively more complex representations, first including just a velocity-dependent drag coefficient, second adding changes in frontal area, and third actively adjusting the local canopy height.

2 Models for canopies in LES

2.1 *Existing distributed drag approaches*

In the present work, we model the momentum equation for conditions without density stratification. Details of sub-grid-scale (SGS) momentum equation are provided by Pan, Chamecki, et al. (2014). The drag force, f_D associated with the canopy elements is parameterized with a distributed drag model:

$$f_D = -C_D(a\mathbf{P}).(\tilde{u}|\tilde{u}|) \tag{1}$$

in which $\tilde{u}$ is the filtered velocity, C_D is the drag coefficient and a is the frontal area per canopy volume, which is equivalent to the one-sided leaf area density. The projected area tensor, $\mathbf{P} = P_x \boldsymbol{e_x e_x} + P_y \boldsymbol{e_y e_y} + P_z \boldsymbol{e_z e_z}$, splits a into the streamwise (x), lateral (y) and vertical (z) directions, where $\boldsymbol{e_j}$ is the unit vector for the j th axis and $\boldsymbol{e_i e_j}$ is the dyadic product between two unit vectors resulting in a second-order tensor. In the original formulation of Eq. (1), C_D is a constant, and $\mathbf{P}$ and a can vary in space, but are fixed in time. To capture the impact of plant reconfiguration on the drag coefficient, Pan, Chamecki, et al. (2014) introduced a velocity-dependent C_D. Specifically, the drag coefficient is specified as a function of the local, instantaneous velocity:

$$C_D = \min\left((|u|/A)^B, C_D^0\right) \tag{2}$$

A is a velocity scale related to canopy geometry and rigidity, and B is the Vogel number (Vogel, 1984, 1989), which describes the rate of drag reduction with increasing velocity due to reconfiguration. C_D^0 is the drag coefficient under conditions with no reconfiguration. The incorporation of this velocity-dependent

drag coefficient by Pan, Chamecki, et al. (2014) significantly improved the simulated skewness for a corn canopy, which is considered an important metric for validating the simulation of canopy-scale coherent structures (Shaw & Seginer, 1987).

2.2 *New approach to model the impact of plant reconfiguration on canopy geometry and drag*

To extend the Pan, Chamecki, et al. (2014) model to seagrass, we note the following difference between the corn and seagrass canopies. For a corn canopy, the canopy height is approximately fixed by the semi-rigid central stem, which does not significantly reconfigure. Therefore, the height of a corn canopy does not change when individual leaves are bending. For this morphology, the impact of leaf reconfiguration can be appropriately modelled by Eq. (2), while keeping the canopy height constant. In contrast, in a seagrass canopy each blade extends over the entire canopy height, so that when the blades reconfigure, the canopy height and vertical distribution of frontal area, **P**, also change. Thus, to properly model the reconfiguration of the seagrass canopy, we must capture the impact of reconfiguration on canopy height, h, and on frontal area distribution, **P**. The details of this new modelling framework are given below.

Two dimensionless parameters govern blade posture in flow. The Cauchy number, Ca, is the ratio of the drag force to the restoring force due to rigidity:

$$Ca = \rho C_D^0 b\tilde{u}^2 l^3/2EI \tag{3}$$

and the buoyancy parameter, R_B, is the ratio between restoring forces due to buoyancy and rigidity:

$$R_B = (\Delta\rho\ g\ bdl^3)/EI \tag{4}$$

Here, l is the blade length, E is the elastic modulus of the blade, d is the blade thickness, $I = bd^3/12$ is the second moment of area assuming a blade with rectangular cross-section, $\Delta\rho$ is the difference in density between the fluid and the blade, and g is the gravitational acceleration. Seagrass material density is $920\,\mathrm{kg\,m^{-3}}$ and a typical value for seawater is $1015\,\mathrm{kg\,m^{-3}}$, so that $\Delta\rho = 95\,\mathrm{kg\,m^{-3}}$.

A model describing the steady-flow-induced reconfiguration of an individual blade as a function of Ca and R_B was described and validated by experimental measurements in Luhar and Nepf (2011). This reconfiguration model was used in the present study to describe the variation in projected frontal area, **P**, as a function of instantaneous velocity within the LES model. The (Luhar & Nepf, 2011) reconfiguration model neglects blade skin friction and assumes that the horizontal velocity is uniform over depth. However, Luhar and Nepf (2011) showed that including the vertical variation in velocity over the canopy height did not significantly change the plant posture. Therefore, in this paper the posture will be predicted using the velocity at the top of the canopy.

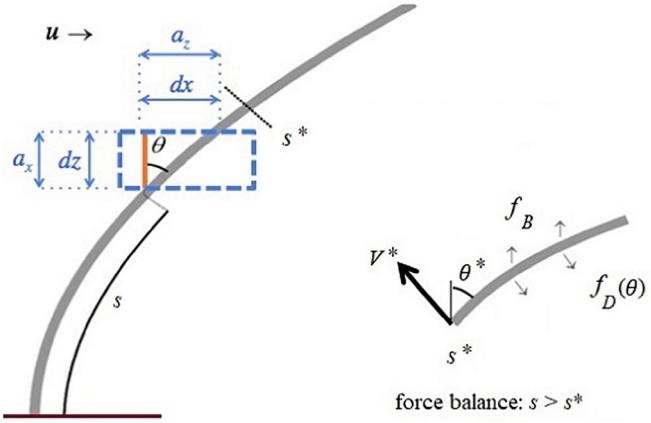

Figure 1 The coordinate system and force balance used to derive the flow induced reconfiguration of a single blade. Blue dashed box with dimensions dx and dz in streamwise and vertical directions, respectively, represents a single grid cell, containing the local projection tensor, P_x and P_z. In the blue box, the vertical red line shows the leaf position when fully erect (no reconfiguration) and θ is the local bending angle of the blade relative to vertical. The right-hand sketch presents the blade-normal force balance for $s \geq s^*$

Luhar and Nepf (2011) predicted the reconfigured blade position in the vertical (z) and streamwise (x) plane based on the balance between drag, rigidity and buoyancy. The lateral projection of the plant is neglected ($P_y = 0$), as the blade thickness (d) is negligibly small compared to the blade length (l) and width (b), and it is assumed that the blades do not twist. The drag force per length along the blade is defined with a quadratic law, $f_D = 1/2\rho C_D b\tilde{u}|\tilde{u}|\cos^2\theta$, in which θ is the local angle between the blade and vertical ($\theta = 0$ denotes upright posture, Fig. 1).

The drag force is resisted through blade stiffness and blade buoyancy. With s the distance along the blade and $s = l$ at the blade tip, the restoring force due to blade stiffness is $V = -EI(d^2\theta/ds^2)$. The vertical buoyancy force per blade length is $f_B = \Delta\rho\ g\ b\ d$. The blade posture is predicted from the balance of these three forces:

$$-\frac{d^2\theta}{ds^2} + R_B(1 - s*)\,sin\,\theta^* = Ca\int_{s^*}^{1} cos\,(\theta - \theta^*)\,cos\,\theta\ ds \tag{5}$$

in which s^* and θ^* are arbitrary position and angle along the blade, respectively. The force balance is the same as that presented in (Luhar & Nepf, 2011). This force balance yields the governing equation for posture: Eq. (6) determines the bending angle along the blade, $\theta(s)$, as a function of Ca and R_B, which was then converted to $\theta(z)$ and used to define the projected areas, P_x and P_z, as functions of the vertical coordinate, z. First, the local leaf area density, a, was defined from the leaf area density of the undeflected canopy, a_0, and the local leaf angle $\theta(s)$ as:

$$a = a_0/cos\,(\theta) \tag{6}$$

Given this adjusted leaf area density within each grid box (blue box in Fig. 1), we can define the leaf area projected in the

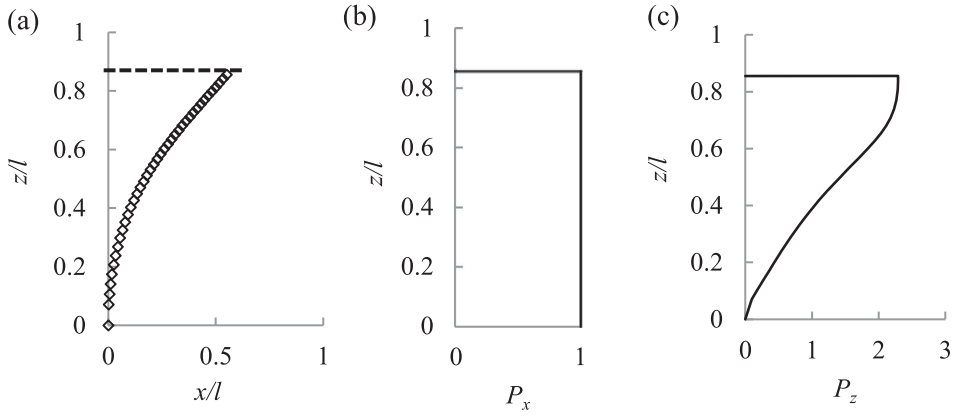

Figure 2 An example of (a) the position of the blade in the x–z plane; (b) P_x and (c) P_z for seagrass case F3, with $Ca = 31$, predicted from the velocity at the canopy top and Eq. (5). The vertical axis is normalized by undeflected canopy height, l, which is also the blade length. The horizontal dashed line in (a) indicates the deflected height of the canopy, h

vertical plane, a_x, and in the horizontal plane, a_z:

$$a_x = a\,cos\,(\theta) = a_0 \tag{7}$$

$$a_z = a\,sin(\theta) = a_0\,tan\,(\theta) \tag{8}$$

Recall that the LES model defines the frontal area in terms of a_0 (Eq. 1), e.g. $a_x = a_0 P_x$ and $a_z = a_0 P_z$. Then, using Eq. (2), $P_x = 1$ and $P_z = tan\ (\theta)$. Further, the deflected canopy height, h, was defined as the maximum vertical coordination of the blade. Above $z = h$, $P_x = P_z = 0$. These definitions conserve the total surface area per bed area ($a_0\ h_0$), i.e. the vertical integral of total leaf area was independent of reconfiguration, $\int_{z=0}^{h} (a_x^2 + a_z^2)^{1/2}\ dz = a_0 h_0$. Plant posture was calculated at each time-step and at each horizontal position in the meadow to update the deflected canopy height, h, and the profiles of P_x and P_z. Figure 2a shows an example of blade posture. With no reconfiguration $P_z = 0$, and $P_x = 1$ over the undeflected canopy height, $h_0 = l$. With reconfiguration, $P_x = 1$, but only over the deflected height, h, and P_z increases from $P_z = 0$ at the bed to a maximum at the top of the deflected canopy. Above the deflected canopy height (marked with horizontal dashed line in Fig. 2) both P_x and $P_z = 0$.

In addition to impacting canopy geometry (h and **P**), the reconfiguration of individual blades also impacts the instantaneous drag coefficient, or specifically the Vogel exponent (B) in Eq. (2). Luhar and Nepf (2011, 2013) described the drag on a reconfigured blade using an effective blade length, l_e, which is the length of rigid, vertical blade that provides the same drag as the reconfigured flexible blade of length l. That is, for a reconfigured blade:

$$f_D = (1/2)\rho C_D^0 b\, l_e\, |\tilde{u}|^2 \tag{9}$$

Note that, in contrast to Pan's formulation (Eqs 1 and 2), the drag coefficient here is held constant at its highest value (C_D^0), and the impact of reconfiguration is captured by the effective length, l_e. As velocity increases, the blade bends further in the streamwise direction, decreasing the blade frontal area and forming a more streamlined shape. Both of these changes reduce the drag and are reflected in the decreasing value of le/l. Equating Eq. (9) to Eqs (1) and (2) leads to:

$$l_e/l = C_D/C_D^0 \sim \tilde{u}^B \sim Ca^{B/2} \tag{10}$$

with $\tilde{u}$ the streamwise component of the resolved velocity vector $\tilde{u}$.

Measurements from Ghisalberti and Nepf (2006) were used to confirm that the scaling laws developed for individual blades in Luhar and Nepf (2011) extended to blades within a meadow. The dependence of canopy drag coefficient on time-mean Ca (Fig. 3) was determined using the six flexible canopy conditions (F1–F6) reported in Table 1 and compared to the dependence measured for individual blades in Luhar and Nepf (2011). The drag coefficient C_D was estimated by dividing the value of $C_D\ a_0$ given in Table 1 of Ghisalberti and Nepf (2006) with the reported value $a_0 = 0.052\,\mathrm{cm}^{-1}$. No reconfiguration was observed in case F1, so that the drag coefficient measured in this

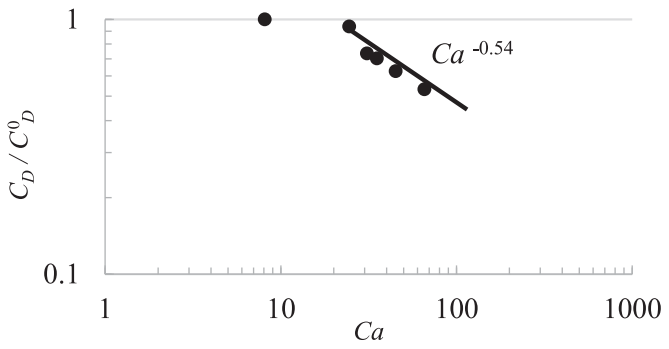

Figure 3 The time-mean drag coefficient, C_D, normalized by the drag coefficient of a blade with no reconfiguration, C_D^0, shown as a function of Cauchy number, Ca. The measurements (solid dots) are taken from flexible canopy runs F1–F6 in Ghisalberti and Nepf (2006). The solid line shows the dependence observed for individual blades ($Ca^{-0.54}$) observed in Luhar and Nepf (2011)

Table 1 Experimental cases from Ghisalberti and Nepf (2006)

Experimental cases	$Q(\times 10^{-2}\ \mathrm{cm^3\ s^{-1}})$	$a_0\ (\mathrm{cm^{-1}})$	H (cm)	h_0 (cm)	$u_*\ (\mathrm{cm\ s^{-1}})$	$\mathsf{R_e}$
R9 Rigid canopy	48	0.08	46.7	13.8	0.54	2565
F3 Flexible canopy	66	0.052	46.7	20.0	0.62	2945

case was assumed to correspond to the rigid drag coefficient, $C_D^0 = 1.23$. The Cauchy number (Ca, Eq. 3) was calculated using $C_D^0 = 1.23$ and the time-mean velocity at the top of the canopy. As shown in Fig. 3, C_D/C_D^0 followed a power-law dependence with Ca, consistent with Eq. (10). Specifically, over the range $Ca = 20.4$ (F2) to 43.8 (F4), C_D/C_D^0 exhibited a power law dependence with Ca with exponent -0.5 ± 0.1, which indicates a Vogel exponent $B = -1.1 \pm 0.2$. This is consistent with the exponent observed for individual blades over the same Ca range (-0.54, in fig. 2c in Luhar & Nepf, 2011), which also indicated $B = -1.1$. This comparison confirmed that the velocity (Ca) dependence of the drag coefficient in a canopy is the same as for a single blade. Note that Fig. 3 represents the steady drag associated with steady reconfiguration under time-mean flow. However, we suggest that the instantaneous drag coefficient follows a similar velocity dependence, which will be used within the numerical model. Specifically, the instantaneous drag model will use Vogel number $B = -1.1$ in Eq. (2). Finally, based on measurements provided in Ghisalberti and Nepf (2006) and shown in Fig. 3, we estimated $A = 0.03\ \mathrm{m\ s^{-1}}$ in Eq. (2), which is the velocity at which reconfiguration begins.

3 Experimental data and simulation cases

In this section we describe the available experimental data and simulation set-up. The measured data were taken from Ghisalberti and Nepf (2006), which included experiments using both rigid and flexible model canopies (details given below). The numerical model was first run with a rigid canopy, representing Run R9 in Ghisalberti and Nepf (2006). Next, the numerical model was run with a flexible canopy (Run F3 in Ghisalberti & Nepf, 2006), with the drag and canopy posture represented by the following three models of increasing complexity:

- Case i: The rigid-canopy model consisted of Eq. (1) with C_D and $P(z)$ fixed in time. C_D was obtained from the experimental data. The canopy height, h, as well as the projections P_x and P_z were constant in time.
- Case ii: The flexible canopy model with velocity-dependent C_D model used Eqs (1) and (2) with $B = -1.1$ and $A = 0.03\ \mathrm{m\ s^{-1}}$. The deflected canopy height, h, as well as deflected projections P_x and P_z were constant in time and calculated based on the time-mean velocity at the top of the canopy.
- Case iii: The flexible canopy model with velocity-dependent C_D and $\mathbf{P}$ used Eqs (1) and (2) with $B = -1.1$ and $A = 0.03\ \mathrm{m\ s^{-1}}$. The time-varying canopy height, $h(x, y, t)$, and projected area tensor, $\mathbf{P}(x, y, z, t)$, were estimated from the blade reconfiguration model using the instantaneous velocity at the top of the canopy.

3.1 *Validation data*

The LES model simulated two cases from Ghisalberti and Nepf (2006), a rigid canopy (Run R9) and a flexible canopy (Run F3). F3 was selected because unsteady reconfiguration, i.e. *monami*, was observed for this case. The flow depth (H) and channel width were 46.7 cm and 38 cm, respectively. The rigid canopy (R9) consisted of randomly arranged wooden cylinders (diameter 0.64 cm) with a frontal area per volume $a_0 = 0.08\ \mathrm{cm^{-1}}$, and canopy height $h_0 = 13.8$ cm, so that $a_0\ h_0 = 1.1$, representative of a dense aquatic canopy, for which KH vortices formed, but for which turbulent sweeps did not penetrate through the entire height of the canopy (Nepf, 2012). The flexible canopy had a plant density of 230 plants $\mathrm{m^{-2}}$. Each plant was constructed with a 1-cm wooden stem and six flexible blades ($l = 20$ cm, width $b = 0.38$ cm, thickness $d = 0.02$ cm) cut from low-density polyethylene. Assuming all blades are seen by the flow, $a_0 = 0.052\ \mathrm{cm^{-1}}$, so that $a_0\ h_0 = 1.07$, also corresponding to a dense canopy ($a_0\ h_0 > 0.1$). The flexible model canopy was geometrically and dynamically similar to the seagrass *Zostera marina* (Ghisalberti & Nepf, 2002).

The instantaneous streamwise, lateral and vertical components of velocity are defined as $\boldsymbol{u} = (u, v, w)$, respectively. Let $\bar{u}$ be the time-average velocity, and then $u'(t) = u(t) - \bar{u}$ is the fluctuating component of velocity, and similarly for the vertical (w) and lateral (v) velocity. Following standard practices in LES studies, the Reynolds stress (RS) is determined using the resolved and sub-grid scale (SGS) parts of the velocity field. However, the standard deviations and skewnesses of the velocity are determined based only on the resolved scales. The skewness of u is $Sk(u) = \overline{u'^3}/{\sigma_u}^3$, in which σ_u is the standard deviation of streamwise velocity u, and similarly for $Sk(w)$.

3.2 *Simulation set-up*

The simulations were done with the incompressible LES code developed by Albertson and Parlange (1999) and more recently advanced by Bou-Zeid, Meneveau, and Parlange (2005) and Chamecki, Meneveau, and Parlange (2009). This LES model has been vetted in a large number of peer-reviewed publications for a range of applications, including channel flow (e.g. Bou-Zeid et al., 2005), atmospheric boundary layer flows (e.g. Kumar, Kleissl, Parlange, & Meneveau, 2006), corn canopy

flow (Pan, Chamecki, et al., 2014), and wind-farms (e.g. Calaf, Parlange, & Meneveau, 2011). The model solves the three-dimensional filtered momentum equation using a fully de-aliased, pseudo-spectral approach in the horizontal directions and a second-order centred finite-difference scheme in the vertical direction. The flow is driven by an imposed time-mean pressure gradient. Viscous effects are neglected due to the large Reynolds number ($\mathrm{R_e}$), and the equations are closed using the Lagrangian scale-dependent dynamic SGS model (Bou-Zeid et al., 2005). A symmetry boundary condition was imposed at the top boundary, and a log-law wall model was applied at the bottom boundary. The bottom boundary condition for horizontal velocity components is represented by a wall model (Bou-Zeid et al., 2005) with an imposed roughness length scale $z_0 = 0.02$ cm following the studies of Yan et al. (2017). Lateral boundary conditions were periodic. Buoyancy effects were neglected. The simulation domain $Lx \times Ly \times Lz$ was set to $6H \times 3H \times H$. A mesh study compared solutions using three grids: $50 \times 50 \times 48$, $100 \times 100 \times 96$ and $200 \times 200 \times 192$, and determined that the model discretization of $100 \times 100 \times 96$ grid points was sufficient since higher grid resolution did not change the results significantly (Fig. S1 and Table S1 in online supplemental data). The grid (Δx, Δy, Δz) was uniform in three directions, with the first vertical grid located $\Delta z/2$ from the wall. To match experimental conditions, the water depth, H, was 3.5 h_0 for the rigid canopy and 2.7 h_0 for the flexible canopy. The simulated canopy covered the entire horizontal domain. Each simulation consisted of a 2-min spin-up time to reach statistically steady-state conditions, followed by another 4 min used for data collection. The eddy turnover time was approximately 30 s, calculated as the vertical domain size divided by the friction velocity at the canopy top, defined as $u_* = \overline{u'w'}^{1/2}|_{z=h}$. For the rigid and flexible canopies, $u^* = 0.54\,\mathrm{cm\,s^{-1}}$ and $u^* = 0.62\,\mathrm{cm\,s^{-1}}$, respectively.

4 Results and discussion

This section describes a set of simulations in which the drag model complexity was progressively increased to understand which level of complexity was needed to achieve good modelling results.

4.1 *Validation with rigid canopy measurements*

Because the rigid canopy was comprised of rigid cylinders, a constant drag model was used ($C_D = 0.8$ based on Ghisalberti & Nepf, 2006) and a constant projection tensor, $P_x = 1$, $P_z = 0$. The constant canopy height was $h_0 = 13.8$ cm, and $a_0\ h_0 = 1.1$. The simulation was evaluated based on velocity and RS (Fig. 4), which were reproduced fairly well by the simulation. The main discrepancy was the over-prediction of streamwise velocity above the rigid canopy. This can be attributed to the presence of secondary circulations within the experimental channel that were not recreated in the simulated channel because of the periodic lateral boundary conditions, as demonstrated in a recent study of secondary circulations with rigid canopies (Yan et al., 2017). The modelled flow velocity was under predicted inside the canopy. This was likely due to assumptions associated with the wall model (e.g. choice of roughness length). The simulations produced excellent agreement with the RS measurements both within and above the canopy. In particular, the model captured the sharp peak in RS at the canopy top. Plots of the skewness also show a reasonable agreement with the experimental data. Because modelling rigid canopies is not the main goal of the present paper, we consider this agreement satisfactory and move to the flexible canopy.

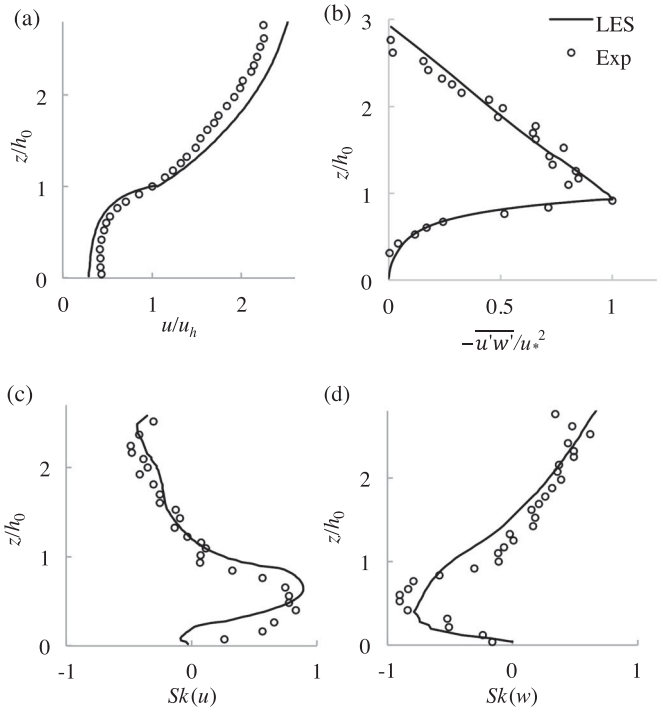

Figure 4 Comparison of LES simulation (solid line) and experimental measurements (circles) for rigid canopy studied in Ghisalberti and Nepf (2006). Vertical coordinate normalized by canopy height, z/h_0. (a) Streamwise velocity, u normalized by velocity at the top of the canopy (u_h); (b) Reynolds stress (RS $= -\overline{u'w'}$ normalized by ${u_*}^2$); (c) and (d) are the skewness in u and w directions, respectively

4.2 *Modelling the flexible canopy*

Table 2 summarizes the numerical set-up and modelling statistics for the flexible canopy cases. Figure 5 compares simulation Case i, which used the rigid canopy approximation, and simulation Case ii, which used a velocity-dependent C_D, but constant **P**, with the measured flow statistics. In both cases the modelled streamwise velocity was overestimated at the top of the canopy, which, as noted above, can be attributed to the lack of secondary circulations within the simulation. The velocity was also over-predicted within the canopy. Importantly, and in agreement with Pan, Chamecki, et al. (2014), there was an insignificant

Table 2 Flexible canopy simulation test cases, variables, and time-averaged statistics

	C_D	Canopy height	Projection tensor	RMSE comparison with observations			
				u/u_*	$\overline{u'w'}/u_*^2$	$Sk(u)$	$Sk(w)$
(i) Constant C_D and **P**	0.9	$h_0 = 17.3$ cm	Mean deflection	0.17	0.23	0.34	0.31
(ii) Velocity-dependent C_D, constant **P**	$C_D = \min((\lvert\boldsymbol{u}\rvert/A)^B, C_D^0)$ $C_D^0 = 0.9$ $B = -1.1$ $A = 0.03\,\mathrm{m\,s^{-1}}$	$h_0 = 17.3$ cm	Mean deflection	0.16	0.23	0.30	0.28
(iii) Velocity-dependent C_D and **P**		Time-varying h (x, y, t)	Time-varying **P** (x, y, t)	0.08	0.10	0.19	0.17

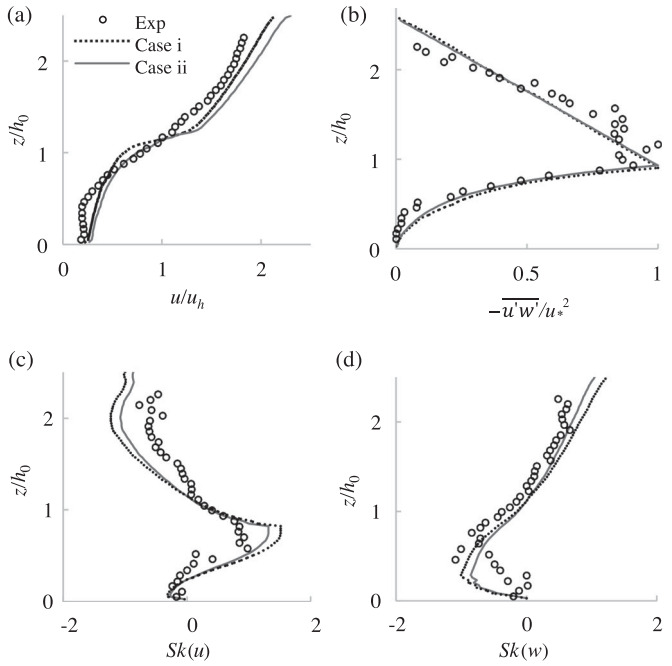

Figure 5 Comparison of simulation (solid and dashed curves) and experimental measurement (circles, Ghisalberti & Nepf, 2006) for Case (i) with steady, deflected canopy and constant C_D (dashed black curves), and Case (ii) with velocity-dependent C_D (solid grey curves). (a) Streamwise velocity normalized by velocity at the top of the canopy; (b) Reynolds stress normalized by u_*^2; (c) and (d) skewness in u and w directions, respectively

change in simulated RS when C_D was changed from a constant (Case i) to a velocity-dependent parameter (Case ii). Further, in both cases the simulated RS profiles had a sharp peak near the top of the canopy, similar to the rigid canopy simulation, but which did not agree with the observed RS profile. The measured RS profile had a broad peak distributed over the vertical distance 0.94 h_0 to 1.4 h_0 ($h_0 = 17.3$ cm). Finally, $Sk(u) > 0$ and $Sk(w) < 0$ inside the canopy, showing the importance of sweeps ($u' < 0$, $w' > 0$) in the downward momentum flux. There was better agreement with observations in Case ii, with a velocity-depended C_D, than Case i, with a constant C_D, indicating that the introduction of a velocity-dependent drag coefficient improved the prediction of skewness within the canopy, similar to the results in Pan's corn canopy (Pan, Chamecki, et al., 2014; Pan, Follett, Chamecki, & Nepf, 2014). The root mean square error (RMSE) was calculated to provide a quantitative comparison between simulation and measured data (Table 2). With regard to RS, Case i and Case ii have the same RMSE = 0.23, and both simulations produced sharp peaks in RS that were not consistent with the measured profile of RS. The RMSE value for skewness improved slightly with the introduction of velocity-dependent C_D, as was also noted in Pan, Follett, et al. (2014). Both simulations produced a peak in $Sk(u)$ that was closer to the top of the canopy than the observed peak skewness. This indicated that sweeps penetrated more deeply into the real canopy compared to the LES simulation. To summarize, this comparison of simulation Case i, using the rigid canopy approximation, and simulation Case ii, using a velocity-dependent C_D, indicated that the velocity-dependent C_D did not significantly improve the simulation. As we will see in the next section, it is only through the introduction of velocity-dependent posture that significant improvement can be achieved.

Finally, we consider simulation Case iii, which incorporated velocity- (and thus time- and spatial-) dependent models for canopy height (h), projection tensor (**P**) and drag coefficient (C_D). Figure 6 compares the simulated and measured velocity statistics. The RMSE for the velocity was reduced from 0.16 to 0.08 between Case ii to Case iii (Table 2). The simulation still over-predicted the near-surface velocity, because the model neglected secondary circulations. The introduction of velocity-dependent h and **P** significantly improved the agreement with measured RS. The RMSE for RS decreased from 0.23 to 0.10 for Case ii to Case iii. Importantly, the Case iii simulation captured the vertical spread of peak RS, which was associated with the fluctuations of the canopy height induced by plant reconfiguration. Measured and computed values of σ_u/u_* and σ_w/u_* are shown in Fig. 6e and 6f, respectively. There was an improvement in the simulation of σ_u/u_* and σ_w/u_* from Case ii (RMSE = 0.33 and 0.12 for σ_u/u_* and σ_w/u_*, respectively) to Case iii (RMSE = 0.16 and 0.07 for σ_u/u_* and σ_w/u_*, respectively). This illustrated that the new flexible

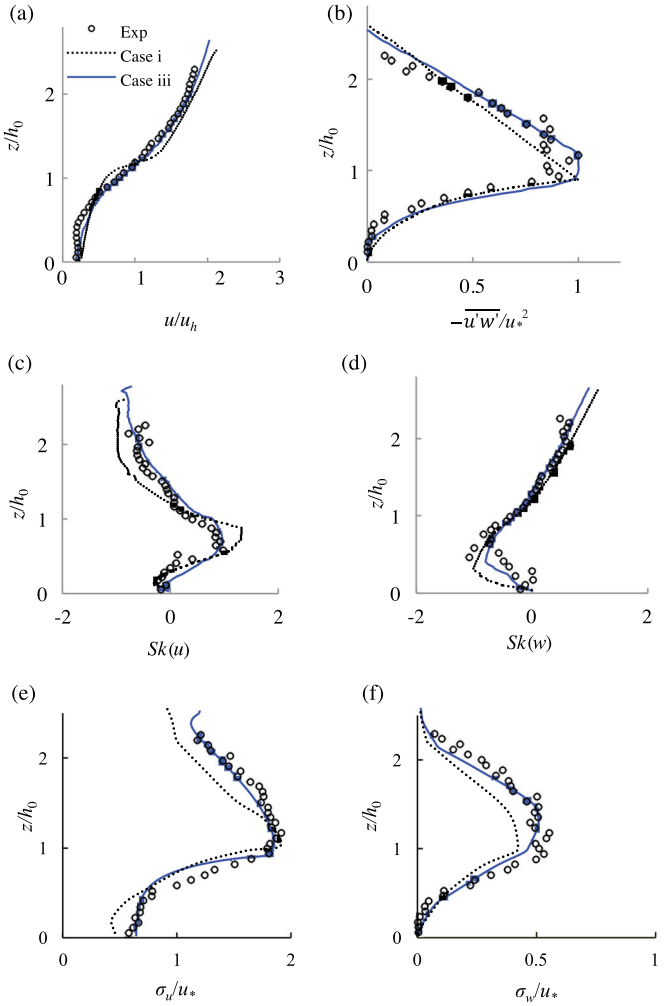

Figure 6 Comparison of experimental measurements (circles, Ghisalberti & Nepf, 2006) and simulation Case (i) with C_D constant and **P** fixed in time (dashed line) and simulation Case (iii) with a velocity-dependent C_D, **P** and h (blue line). Vertical coordinate (z) normalized by time-mean canopy height h_0. (a) Streamwise velocity, u, normalized by velocity u_h at the top of the canopy; (b) Reynolds stress normalized by ${u_*}^2$; (c) skewness in u direction; (d) skewness in w direction; (e) σ_u and (f) σ_w, normalized by the u_*

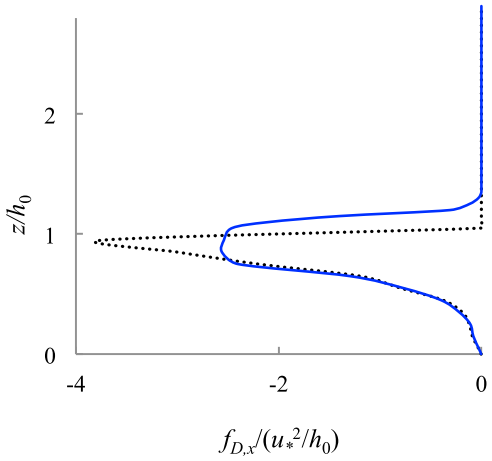

Figure 7 Distributed drag, $f_{D,x}$, normalized by ${u_*}^2/h_0$ for simulation Case ii (dashed black line) and Case iii (blue line)

canopy model was better able to reproduce resolved velocity components, indicating that the main turbulent kinetic energy (TKE) production and dissipation mechanisms are properly represented in the LES simulation. Finally, for cases with a constant canopy height (e.g. Case ii), a jump discontinuity was observed in the mean drag force distribution (Fig. 7). Case ii, which has a constant canopy height, had a much sharper change in the drag force than Case iii, for which the canopy height varied in time, i.e. the position of the drag-discontinuity varied in time. This was consistent with the observations of RS, i.e. when the movement of the canopy interface was represented in the simulation (Case iii), the vertical spread of the peak RS was properly captured, as opposed to the sharp peak simulation in Case ii.

The velocity-dependent C_D, h and **P** model (Case iii) predicted the peak in skewness to within 10% (maximum $Sk(u) = 0.90$ for simulation and $= 0.98$ for experiment). In addition, the RMSE for $Sk(u)$ was reduced from 0.30 to 0.19 between simulation Case ii and Case iii. The peak in $Sk(u)$ was also located deeper in the canopy for the velocity-dependent C_D, **P** and h simulation (Case iii), in better agreement with the measurements. Specifically, in simulation Case ii, with constant canopy height, the peak skewness was 0.18 h_0 below the canopy top, but in Case iii, with velocity-dependent C_D h and P, this distance increased to 0.40 h_0, which was closer to the measured position of peak skewness (0.42 h_0 below canopy top). This indicated that the time-variable canopy height and projection tensor were important elements in recreating realistic plant and eddy interaction. The magnitude of $Sk(w)$ had the largest deviation from the measurement (RMSE $= 0.28$ and 0.17 in Case ii and Case iii, respectively). Although the peak value of $Sk(w)$ was underestimated in the simulation (maximum $Sk(w) = -0.6$ and -1.0 in the simulation and observation, respectively), the model correctly predicted the location of the peak $Sk(w)$, located at $z/h = 0.45$ and 0.51 for LES simulations and observations, respectively.

The runs with velocity-dependent canopy posture (Case iii) also captured the progressive waving of the canopy, known as *monami*. The time-mean and root mean square values of simulated canopy height are $h_0 = 16.8$ cm and $h_{rms} = 1.6$ cm, respectively. The root mean square (rms) canopy height corresponded to a *monami* amplitude $A_w = \sqrt{2}h_{rms} = 2.3$ cm, which agreed with the *monami* amplitude observed in Ghisalberti and Nepf (2006), $A_w = 2.7 \pm 0.7$ cm. Further, Ghisalberti and Nepf (2006) reported a *monami* period of about 16 s. The simulated *monami* period was 12.5 s (Fig. 8b). The difference in canopy height from the mean-deflected height, Δh, is presented in top view (x–y plane) in Fig. 8a for one instant in time. The spatial variation in canopy height illustrates the streamwise length-scale of the *monami*, which was set by the coherent KH structures moving along the canopy top. The periodic structure

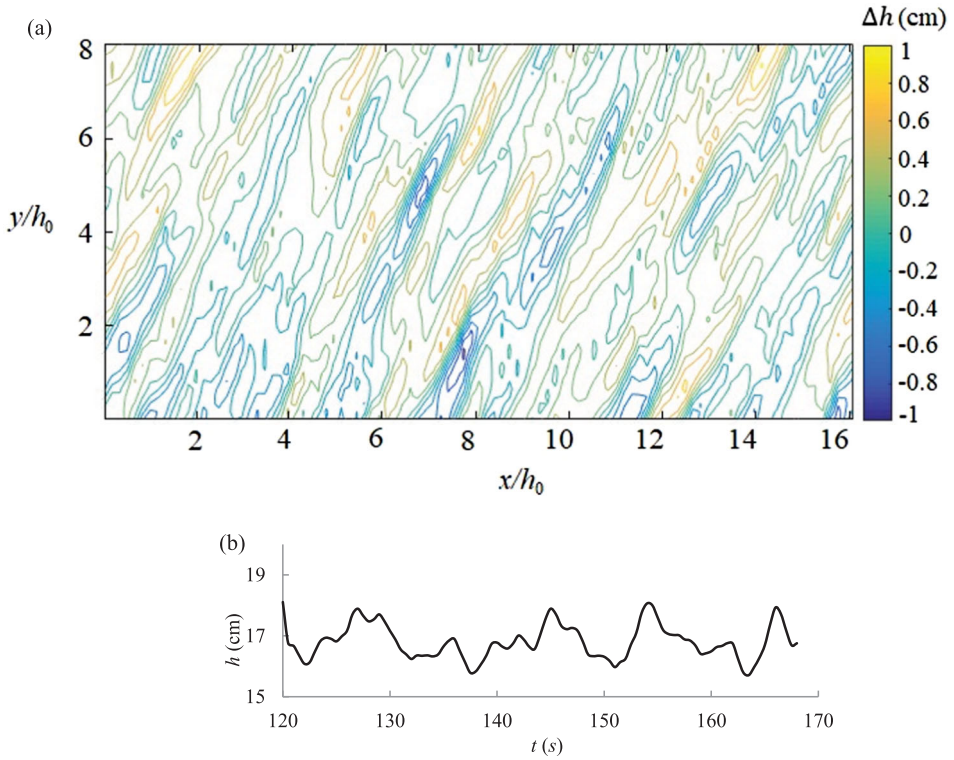

Figure 8 (a) Snapshot of simulated canopy height described by deviation, $\Delta\, h$, from time-mean deflected height in Case iii simulation. Streamwise (x) and lateral (y) dimensions normalized by the h_0; (b) simulated time history of deflected height h (t) at the centre of canopy ($x = 1.5$ m, $y = 0.75$ m) in Case iii simulation

in canopy height had a streamwise length-scale of (3.0 ± 0.4) h_0. This value was estimated by averaging the last 2 min of the simulation and over the entire horizontal domain. Figure 8a also reveals a lateral structure in the canopy motion. Specifically, the canopy height varies over the width of the channel with a length–scale of (1.7 ± 0.3) h_0. This lateral variation in *monami* phase is associated with the three-dimensional nature of the KH vortices that is generated by a secondary instability that segments the originally 2-D structures into individual sub-channels that have the same vortex size and speed, but different phase (Ghisalberti & Nepf, 2002). For example, Fig. 3 of Ghisalberti and Nepf (2004) illustrated the existence of two sub-channels. Specifically, closer to the camera a vortex is sweeping tracer downward into the canopy, but at the same time tracer is ejected (carried upward) from the canopy by a vortex in the neighbouring sub-channel that is out of phase with the vortex closer to the camera. In flexible canopies this lateral structure in the KH vortices is expressed as a lateral variation in canopy waving. Ghisalberti and Nepf (2002) observed three *monami* streets in their submerged flexible canopy. Similarly, Fig. 8a indicated three vortex streets, with the canopy height at the centre of the channel out of phase with the canopy height at the sides of the channel, which are in phase with one another. The progressive waving within each street has the same frequency, but different phase, causing lateral non-uniformity. Similar observations have also been reported in terrestrial canopies (Finnigan, 2000). Figure 8a demonstrates that the LES simulation captured the evolution of KH vortices into discrete sub-channels and their impact on canopy waving.

The propagation velocity of the coherent, shear-layer structures at the canopy height, u_v, was estimated from the simulated spatial-scale $(3.0 \pm 0.4)h_0$ and temporal-scale (12.5 s) of the canopy waving, which gives $u_v = 4.0 \pm 0.5\,\mathrm{cm\,s^{-1}}$. Normalizing by the time-mean velocity at the time-mean canopy interface, $u_h = 2.2\,\mathrm{cm\,s^{-1}}$, yielded $u_v/u_h = 1.8 \pm 0.2$. This value is consistent with measurements made for a model seagrass, $u_v/u_h = 1.4$ to 1.7 (reported in Table 4 in Ghisalberti & Nepf, 2002). In addition, the values are comparable to observations made for a wheat canopy, $u_v/u_h = 1.6$ to 2.5 (Fig. 16 in Finnigan, 1979). This indicated that the convection of simulated shear-layer structures in our study was consistent with observations of flexible submerged canopies and canopies in terrestrial environment, suggesting a universal behaviour.

5 Concluding remarks

Several studies have advanced our understanding of plant–flow interaction using plant-resolving simulations (e.g. Ikeda et al., 2001; Marjoribanks et al., 2014); however, these simulations are not computationally practical at large scale. This paper proposed a new approach that will facilitate simulation

of meadows at field-scale. Specifically, this paper advanced the distributed-drag approach for modelling plant–flow interaction by incorporating velocity-dependent models for both canopy morphology and drag. The velocity-dependent models for drag coefficient (C_D), canopy height (h) and frontal area projection tensor ($\mathbf{P}$) were based on physical experiments and scaling laws describing the time-mean reconfiguration of individual flexible blades (Ghisalberti & Nepf, 2006; Luhar & Nepf, 2011). Building on the successful application of velocity-dependent drag coefficients for corn canopies (Pan, Chamecki, et al., 2014; Pan, Follett, et al., 2014), our study first considered only the addition of a velocity-dependent drag coefficient for modelling seagrass. However, because of the greater flexibility and reconfiguration of seagrass blades (compared to corn plants), the velocity-dependent drag coefficient only produced small improvements in the agreement between measured and simulated velocity statistics. By additionally including velocity-dependent canopy height, h, and area projection tensor, $\mathbf{P}$, the simulation of velocity statistics was significantly improved. In particular, unlike all previous models, the new velocity-dependent canopy posture model captured the observed vertical spread in peak RS that is associated with the movement of the canopy interface. Further, the statistics of time-varying canopy height matched observed values. The new model accurately incorporated the impact of plant reconfiguration on time-varying canopy drag and time-varying canopy morphology (h, $\mathbf{P}$) within the context of a distributed-drag model, providing a method to represent flexible canopies at a much lower computational cost than plant-resolving methods. Given the recent recognition of coastal vegetation as an important natural defence against storm surge and waves, this model addresses an urgent need for better tools to predict the potential storm protection provided by seagrass. Further, an improved model for flow through seagrass is an important tool for managing existing seagrass stocks and planning the restoration of seagrass.

Acknowledgements

The research reported here was carried out with the support of the Swiss National Science Foundation [grant P2ELP2_158885].

Funding

The research reported here was carried out with the support of the Swiss National Science Foundation [grant P2ELP2_158885]; Schweizerischer Nationalfonds zur Förderung der Wissenschaftlichen Forschung.

Supplemental data

Supplemental data for this article can be accessed doi:10.1080/00221686.2019.1671511.

Notation

A	=	velocity scale at which reconfiguration is initiated, related to canopy geometry and rigidity ($\mathrm{m\,s^{-1}}$)
A_w	=	monami amplitude (m)
a	=	total vegetation frontal area per unit canopy volume ($\mathrm{m^{-1}}$)
a_0	=	leaf area density of the undeflected canopy ($\mathrm{m^{-1}}$)
a_x and a_z	=	frontal area per volume with reference to in streamwise (x) and vertical (z) directions ($\mathrm{m^{-1}}$)
B	=	Vogel number, which is an exponent describing the velocity dependence of the drag (−)
b	=	blade width (m)
Ca	=	Cauchy number, ratio of the drag force to the restoring force due to rigidity (−)
C_D	=	drag coefficient (−)
C_D^0	=	drag coefficient for the undeflected canopy (−)
d	=	blade thickness (m)
E	=	elastic modulus of the blade ($\mathrm{kg\,m^{-1}\,s^{-2}}$)
$\boldsymbol{e_x}$, $\boldsymbol{e_y}$ and $\boldsymbol{e_z}$	=	unit vectors in streamwise, lateral and vertical axes (−)
f_D	=	drag force ($\mathrm{kg\,m\,s^{-2}}$)
$f_{D,x}$	=	drag force in the streamwise direction ($\mathrm{kg\,m\,s^{-2}}$)
f_B	=	vertical buoyancy force per blade length ($\mathrm{kg\,m\,s^{-2}}$)
g	=	gravitational acceleration ($\mathrm{m\,s^{-2}}$)
H	=	water depth (m)
h	=	canopy height (m)
h_{rms}	=	root mean square (rms) canopy height (m)
h_0	=	canopy height without bending (m)
I	=	bending moment of bladec ($\mathrm{m^{-4}}$)
l	=	blade length (m)
l_e	=	effective blade length (m)
Lx, Ly and Lz	=	simulation domain in streamwise, lateral and vertical directions (m)
$\mathbf{P}$	=	projection tensor (−)
P_x, P_y and P_z	=	streamwise, lateral and vertical projection of the blade (−)
$\tilde{\rho}$	=	filtered pressure ($\mathrm{kg\,m^{-1}\,s^{-2}}$)
Q	=	discharge ($\mathrm{m^3\,s^{-1}}$)
R_B	=	ratio between restoring forces due to buoyancy and rigidity (−)
$\mathsf{R_e}$	=	Reynolds number (−)
RS	=	$-\overline{u'w'}$ = Reynolds stresses
s and s^*	=	the distance along the blade and arbitrary position along the blade (m)
$Sk(u)$ and $Sk(w)$	=	skewness in the streamwise velocity and skewness in the vertical velocity (−)

t	=	time (s)
$\boldsymbol{u}$	=	instantaneous flow velocity ($\mathrm{m\,s^{-1}}$)
$\tilde{\boldsymbol{u}}$	=	filtered flow velocity ($\mathrm{m\,s^{-1}}$)
$\bar{u}$	=	time-average velocity ($\mathrm{m\,s^{-1}}$)
u and u'	=	horizontal velocity component and horizontal turbulent fluctuation ($\mathrm{m\,s^{-1}}$)
u_*	=	friction velocity ($\mathrm{m\,s^{-1}}$)
u_h	=	velocity at the top of canopy ($\mathrm{m\,s^{-1}}$)
u_v	=	vortex velocity ($\mathrm{m\,s^{-1}}$)
v	=	lateral velocity component ($\mathrm{m\,s^{-1}}$)
w and w'	=	vertical velocity component and vertical turbulent fluctuation, respectively ($\mathrm{m\,s^{-1}}$)
V	=	blade stiffness ($\mathrm{kg\,s^{-2}}$)
x, y and z	=	streamwise, lateral and vertical coordinates (m)
z_0	=	bed roughness length (m)
$\Delta\,\rho$	=	difference in density between the fluid and the blade ($\mathrm{kg\,m^{-3}}$)
θ	=	local angle between the blade and vertical coordinate ($-$)
$\theta(s)$ and $\theta(z)$	=	local angle between the blade and the vertical coordinate at s and z, respectively ($-$)
θ^*	=	arbitrary angle along the blade ($-$)
ρ	=	water density ($\mathrm{kg\,m^{-3}}$)
σ_u	=	standard deviation of streamwise velocity u ($\mathrm{m\,s^{-1}}$)
σ_w	=	standard deviation of vertical velocity w ($\mathrm{m\,s^{-1}}$)

References

Albertson, J., & Parlange, M. (1999). Surface length scales and shear stress: Implications for land-atmosphere interaction over complex terrain. *Journal of Water Recourses Research*, *35*, 2121–2132.

Barbier, E., Hacker, S., Kennedy, C., Koch, E., Stier, A., & Silliman, B. (2011). The value of estuarine and coastal ecosystem services. *Journal of Ecological Monographs*, *81*(2), 169–193.

Bou-Zeid, E., Meneveau, C., & Parlange, M. (2005). A scale-dependent Lagrangian dynamic model for large eddy simulation of complex turbulent flows. *Journal of Physics of Fluids*, *17*, 025105.

Burke, R., & Stolzenbach, K. (1983). *Free surface flow through salt marsh grass*. MITSG 83-16 Technical Report. Cambridge, MA: MIT.

Calaf, M., Parlange, M., & Meneveau, C. (2011). Large eddy simulation study of scalar transport in fully developed wind-turbine array boundary layers. *Journal of Physics of Fluids*, *23*, 126603.

Chamecki, M., Meneveau, C., & Parlange, M. (2009). Large eddy simulation of pollen transport in the atmospheric boundary layer. *Journal of Aerosol Science*, *40*, 241–255.

Choi, S. U., & Kang, H. (2016). Characteristics of mean flow and turbulence statistics of depth-limited flows with submerged vegetation in a rectangular open-channel. *Journal of Hydraulic Research*, *54*(5), 527–540.

Dupont, S., Gosselin, F., Py, C., De Langre, E., Hemon, P., & Brunet, Y. (2010). Modelling waving crops using large-eddy simulation: comparison with experiments and a linear stability analysis. *Journal of Fluid Mechanics*, *652*, 5–44.

Finnigan, J. (1979). Turbulence in waving wheat, I, Mean statistics and honami. *Journal of Boundary Layer Meteorology*, *16*, 181–211.

Finnigan, J. (2000). Turbulence in plant canopies. *Annual Review of Fluid Mechanics*, *32*, 519–571.

Gerken, T., Chamecki, M., & Fuentes, J. D. (2017). Air-parcel residence times within forest canopies. *Journal of Boundary-Layer Meteorology*, *165*, 29–54.

Ghisalberti, M., & Nepf, H. M. (2004). The limited growth of vegetated shear layers. *Water Resources Research*, *40*, W07502. doi:10.1029/2003WR002776

Ghisalberti, M., & Nepf, H. (2002). Mixing layers and coherent structures in vegetated aquatic flows. *Journal of Geophysical Research*, *107*(C2), 3011.

Ghisalberti, M., & Nepf, H. (2006). The structure of the shear layer in flows over rigid and flexible canopies. *Journal of Environmental Fluid Mechanics*, *6*, 277–301.

Huthoff, F., Augustijn, D. C. M., & Hulscher, S. J. M. H. (2007). Analytical solution of the depth-averaged flow velocity in case of submerged rigid cylindrical vegetation. *Journal of Water Resour. Research*, *43*(6), W06413.

Ikeda, S., Yamada, T., & Toda, Y. (2001). Numerical study on turbulent flow and honami in and above flexible plant canopy. *International Journal of Heat and Fluid Flow*, *22*(3), 252–258.

Katul, G., Poggi, D., & Ridolfi, L. (2011). A flow resistance model for assessing the impact of vegetation on flood routing mechanics. *Journal of Water Resource Research*, *47*, W08533.

Kennedy, H., Beggins, J., Duarte, C., Fourqurean, J., Holmer, M., Marba, N., & Middelburg, J. (2010). Seagrass sediments as a global carbon sink: Isotopic constraints. *Journal of Global Biogeochemical Cycles*, *24*, GB4026.

King, A., Tinoco, R., & Cowen, E. (2012). A k–ϵ turbulence model based on the scales of vertical shear and stem wakes valid for emergent and submerged vegetated flows. *Journal of Fluid Mechanics*, *701*, 1–39.

Kumar, V., Kleissl, J., Parlange, M., & Meneveau, C. (2006). A large-eddy simulation of a diurnal cycle of the turbulent atmospheric boundary layer: Atmospheric stability and scaling issues. *Journal of Water Resource Research*, *42*, W06D09.

Li, C., & Xie, J. (2011). Numerical modeling of free surface flow over submerged and highly flexible vegetation. *Journal of Advances in Water Resources*, *34*(4), 468–477.

Lien, F., Yee, E., & Wilson, J. (2005). Numerical modelling of the turbulent flow developing within and over a 3-d building

array, part ii: a mathematical foundation for a distributed drag force approach. *Journal of Boundary-Layer Meteorology*, *114*(2), 245–285.

Luhar, M., & Nepf, H. (2011). Flow-induced reconfiguration of buoyant and flexible aquatic vegetation. *Limnology and Oceanography.*, *56*(6), 2003–2017.

Luhar, M., & Nepf, H. (2013). From the blade scale to the reach scale: a characterization of aquatic vegetative drag. *Advances in Water Resources*, *51*, 305–316.

Marjoribanks, T., Hardy, R., Lane, S., & Parsons, D. (2014). High-resolution numerical modelling of flow—vegetation interactions. *Journal of Hydraulic Research*, *52*(6), 775–793.

Mattis, S., Dawson, C., Kees, C., & Farthing, M. (2015). An immersed structure approach for fluid-vegetation interaction. *Journal of Advances in Water Resources*, *80*, 1–16.

Nepf, H. (2012). Flow and transport in regions with aquatic vegetation. *Annual Review of Fluid Mechics*, *44*, 123–142.

Nezu, I., & Sanjou, M. (2008). Turburence structure and coherent motion in vegetated canopy open-channel flows. *Journal of Hydro Environment Research*, *2*, 62–90.

Nikora, N., Nikora, V., & Donoghue, T. (2013). Velocity Profiles in Vegetated Open-Channel Flows: Combined Effects of Multiple Mechanisms. *Journal of Hydraulic Engineering*, *139*(10), 1021–1032.

Pan, Y., Chamecki, M., & Isard, S. (2014). Large-eddy simulation of turbulence and particle dispersion inside the canopy roughness sublayer. *Journal of Fluid Mechanics*, *753*, 499–534.

Pan, Y., Follett, E., Chamecki, M., & Nepf, H. (2014). Strong and weak, unsteady reconfiguration and its impact on turbulence structure within plant canopies. *Journal of Physics of Fluids*, *26*, 105102.

Raupach, M., Finnigan, J., & Brunet, Y. (1996). Coherent eddies and turbulence in vegetation canopies: The mixing-layer analogy. *Boundary-Layer Meteorology*, *78*, 351–382.

Shaw, R., & Schumann, U. (1992). Large-eddy simulation of turbulent flow above and within a forest. *Journal of Boundary-Layer Meteorology*, *61*, 47–64.

Shaw, R., & Seginer, I. (1987). Calculation of velocity skewness in real and artificial plant canopies. *Journal of Boundary-Layer Meteorology*, *39*(3), 15–332.

Vogel, S. (1984). Drag and flexibility in sessile organisms. *Journal of American Zoologist*, *24*, 37–44.

Vogel, S. (1989). Drag and reconfiguration of broad leaves in high winds. *Journal of Experimental Botany*, *40*, 941–948.

Waycott, M., Duarte, T., Carruthers, R., Orth, W., Dennison, S., Olyarnik, A., . . . Williams, S. (2009). Accelerating loss of seagrasses across the globe threatens coastal ecosystems. *Proceedings of the National Academy of Sciences*, *106*, 12377–12381.

Yan, C., Nepf, H., Huang, W., & Cui, G. (2017). Large eddy simulation of flow and scalar transport in a vegetated channel. *Journal of Environmental Fluid Mechanics*, *17*, 497–519.